Article:
Wareing, CJ, Fairweather, M, Falle, SAEG et al. (2014) Modelling punctures of buried high-pressure dense phase CO2 pipelines in CCS applications. International Journal of Greenhouse Gas Control, 29. 231 - 247. ISSN: 1750-5836

https://doi.org/10.1016/j.ijggc.2014.08.012

Modelling punctures of buried high-pressure dense phase CO_2 pipelines in CCS applications

Christopher J. Wareing[a,*], Michael Fairweather[a], Samuel A.E.G. Falle[b], Robert M. Woolley[a]

[a]*School of Process, Environmental and Materials Engineering, University of Leeds, Leeds LS2 9JT, UK.*
[b]*School of Mathematics, University of Leeds, Leeds LS2 9JT, UK.*

Abstract

Carbon capture and storage (CCS) presents a short-term option for significantly reducing the amount of carbon dioxide (CO_2) released into the atmosphere and mitigating the effects of climate change. To this end, National Grid initiated the COOLTRANS research programme to consider the pipeline transportation of high pressure dense phase CO_2. Part of this work involved the development of a mathematical model for predicting the near-field dispersion of pure CO_2 following the venting, puncture or rupture of such a pipeline. This article describes the application of this model to the simulation of punctures in buried pipelines, and specifically three scenarios - a puncture at the side, at the base and at the top of the pipeline. Such scenarios following human interference with the pipeline are the most common type of pipeline failure and form an important part of the quantitative risk analysis (QRA) required in the development of such pipelines for CCS. In

*Corresponding author. Tel: +44 113 343 1619. Fax: +44 113 343 5090
Email address: C.J.Wareing@leeds.ac.uk (Christopher J. Wareing)
URL: http://www.maths.leeds.ac.uk/~cjw (Christopher J. Wareing)

each scenario, a idealised crater is modelled, dispersing CO_2 into dry air. In two of the experiments, an idealisation of a naturally formed crater is used. In the third, the idealisation is based on the pre-formed crater. We present the steady state flow in each scenario and, using Lagrangian particle tracking techniques, give estimates on the amount of solid CO_2 deposited in the crater. In the case of the side puncture, experimental data above the crater are available and the model qualitatively and quantitatively predicts the nature of the flow in this case. The validated steady state flows at the top of the crater presented here for these three common scenarios provide the basis for developing robust source conditions for use in computational fluid dynamics (CFD) studies of far-field dispersion and for use with pragmatic QRA models, as well as representing a significant step towards modelling full-scale ruptures of CCS pipelines.
Keywords: CCS Transport, multi-phase flow, experimental measurement, mathematical modelling, accidental releases, atmospheric dispersion

---

1. Introduction

Carbon capture and storage (CCS) refers to a set of technologies designed to reduce carbon dioxide (CO_2) emissions from large point sources of emission, such as coal-fired power stations, in order to mitigate greenhouse gas emission. The technology involves capturing CO_2 and then storing it in a reservoir (sequestration), instead of allowing its release to the atmosphere, where it contributes to climate change. Once captured, the CO_2 is transported and sequestered, typically underground, or used for processes such as enhanced oil recovery (EOR).

National Grid initiated the TRANSportation of Liquid CO_2 research programme (COOLTRANS) (Cooper, 2012) in order to address knowledge gaps relating to the safe design and operation of onshore pipelines for transporting dense phase CO_2 from industrial emitters in the UK to storage sites offshore. This includes developing the capability for modelling accidental releases from a buried pipeline that contains CO_2 in the dense phase and applying the learning from these studies to develop an appropriate quantified risk assessment (QRA) for a dense phase CO_2 pipeline. The programme includes theoretical studies by University College London (UCL), the University of Leeds and the University of Warwick, carried out in parallel to provide "state of the art" models for the outflow, near-field dispersion behaviour and far-field dispersion behaviour associated with below ground CO_2 pipelines that are ruptured or punctured. Experimental work and studies using currently available practical models for risk assessment are being carried out by DNV GL (Allason et al., 2012).

The fluid dynamic modelling of CO_2 poses a unique set of problems due to its unusual phase transition behaviour and physical properties. Liquid CO_2 has a density comparable with that of water, but has a viscosity of magnitude more frequently associated with gases. These properties make the transport of dense phase CO_2 an economically viable and attractive proposition. However, due to it possessing a relatively high Joule-Thomson expansion coefficient, calculations and experimental evidence indicate that the rapid expansion of an accidental release may reach temperatures below -100^{o}C in some circumstances. Due to this effect, solid CO_2 formation following a pipeline puncture or rupture is to be expected, whether directly from liquid

or via a vapour-phase transition. Additionally, CO_2 sublimes at ambient atmospheric conditions, which is a behaviour not seen in most other solids, and is an additional consideration when modelling flows such as these. Predicting the correct fluid phase during the discharge process in the near-field is of particular importance given the very different hazard profiles of CO_2 in the gas and solid states. The safe operation of CO_2 pipelines is of paramount importance then, as the inventory associated with a cross-country pipeline would likely be several thousand tonnes, and CO_2 has a toxic effect above 5% concentration and causes hyperventilation above 2% (Connolly and Cusco, 2007; Wilday et al., 2009).

In this paper, the University of Leeds mathematical model (Wareing et al., 2013a), previously validated for free releases into air (Woolley et al., 2013; Wareing et al., 2014) is now applied to the simulation of punctures of buried pipelines. Specifically, we consider punctures, idealised as circular holes with a 25mm diameter, to pipelines in three scenarios. Firstly, a puncture at the side of the pipeline, secondly a puncture at the base of the pipeline and thirdly a puncture at the top of the pipeline. Whilst the puncture and the outflow conditions remain unchanged between these three scenarios, the crater modelled in each case, based on craters observed in experimental studies, is considerably different. Hence the nature of the flow out of the crater is different between the three cases. The results described in this paper represent a considerable step toward the goal of developing the understanding and modelling capabilities for a range of releases from the rupture of a full-scale buried pipeline. In addition, these scenarios are of considerable interest in their own right as they represent the most common pipeline failure mech-

anism following human interference (Duncan and Wang, 2014). We have previously reviewed relevant work in the literature and we refer the interested reader to our previous work in this area (Wareing et al., 2014). As far as we are aware, this is the first application of an accurate near-field model to a CCS scenario involving a buried pipeline - all previous work considers free expansion into air. As such, any validation of this new model is beneficial and here we are able to compare the simulation of a sideways puncture of a buried pipeline to experimental measurements taken 1m above the crater.

In the next section we summarise the numerical method. Then the application to a sideways puncture of a buried pipeline is presented in Section 3, with validation against experimental measurements in Section 4. The modelling of a puncture at the base of a pipeline is presented in Section 5, followed by the modelling of a puncture at the top of a pipeline in Section 6. A discussion of the implications of these results is given in Section 7, followed by our conclusions in Section 8.

2. Mathematical model and numerical method

The mathematical model and numerical method is the same as that adopted and validated in our earlier papers (Wareing et al., 2013a; Woolley et al., 2013; Wareing et al., 2014) and we refer the reader to these articles for detailed information and validation of our approach. In particular, we develop a numerical equation of state method for pure CO_2 (Wareing et al., 2013a) which we then validate against free jet releases into air in later work (Woolley et al., 2013; Wareing et al., 2014). In this domain of application, we have demonstrated that the experimental data available are accurately

simulated. In the following subsections, we summarise this method and go on to apply it to buried pipelines and below ground releases into craters.

2.1. Reynolds-Averaged Navier-Stokes Mathematical Model

The Reynolds-Averaged Navier-Stokes (RANS) equations, closed with a compressibility-corrected k-ϵ turbulence model, employed in this work are:

$$\frac{\partial \rho}{\partial t} + \nabla \cdot (\rho \mathbf{u}) = 0 \tag{1}$$

$$\frac{\partial \rho C}{\partial t} + \nabla \cdot (\rho C \mathbf{u}) - \nabla \cdot (\mu_T \nabla C) = 0 \tag{2}$$

$$\frac{\partial \rho \mathbf{u}}{\partial t} + \nabla \cdot (\rho \mathbf{u}\mathbf{u}) + \nabla P - \nabla \cdot \tau = \mathbf{s}_p \tag{3}$$

$$\frac{\partial E}{\partial t} + \nabla \cdot [(E + P)\mathbf{u} - \mathbf{u} \cdot \tau] - \nabla \cdot (\mu_T T \nabla S) = 0 \tag{4}$$

$$\frac{\partial \rho k}{\partial t} + \nabla \cdot (\rho k \mathbf{u}) - \nabla \cdot (\mu_T \nabla k) = s_k \tag{5}$$

$$\frac{\partial \rho \epsilon}{\partial t} + \nabla \cdot (\rho \epsilon \mathbf{u}) - \nabla \cdot (\mu_\epsilon \nabla \epsilon) = s_\epsilon \tag{6}$$

where the variables have their usual meanings, noting that the vector velocity is expressed in bold as $\mathbf{u}$ and S is the entropy per unit mass. The turbulent diffusion coefficients are

$$\mu_T = \rho C_\mu \frac{k^2}{\epsilon}, \quad \mu_\epsilon = \frac{\mu_T}{1.3}, \quad C_\mu = 0.09. \tag{7}$$

The momentum equation source term, $\mathbf{s}_p$, is zero in Cartesian coordinates. In axisymmetry it is

$$\mathbf{s}_p = \begin{pmatrix} \mu_T \left[\frac{2}{3r} \nabla \cdot \mathbf{u} - 2\frac{u_r}{r^2} \right] + \frac{1}{r} \left[P + \frac{2}{3r} \rho k \right] \\ \\ 0 \end{pmatrix}. \tag{8}$$

The k source term is

$$s_k = P_t - \rho\epsilon \tag{9}$$

whilst the ϵ source term is

$$s_\epsilon = \frac{\epsilon}{k}(C_1 P_t - C_2 \rho\epsilon), \quad C_1 = 1.4,\ C_2 = 1.94. \tag{10}$$

The turbulence production term is

$$P_t = \mu_T \left[\frac{\partial u_i}{\partial x_j} \left(\frac{\partial u_i}{\partial x_j} + \frac{\partial u_j}{\partial x_i} \right) \right] - \frac{2}{3} \nabla \cdot \mathbf{u} (\rho k + \mu_T \nabla \cdot \mathbf{u}), \tag{11}$$

where the summation convention has been assumed. In axisymmetry, the production term is as above with an extra geometric term

$$2\mu_T \frac{u_r^2}{r^2}. \tag{12}$$

The turbulent stress tensor, τ, is

$$\tau_{ij} = \mu_T \left(\frac{\partial u_i}{\partial x_j} + \frac{\partial u_j}{\partial x_i} \right) - \frac{2}{3} \delta_{ij} (\mu_T \nabla \cdot \mathbf{u} + \rho k). \tag{13}$$

The k-ϵ turbulence model described here is coupled to a compressibility dissipation rate correction proposed by Sarkar et al. (1991). Comparisons of model predictions with this correction and experimental data have shown significant improvements over results derived using the standard k-ϵ approach for moderately and highly under-expanded jets of the type under consideration here (Cumber et al., 1994, 1995).

2.2. Equation of State

The composite equation of state recently described in Wareing et al. (2013a) is employed. This composite method predicts the thermophysical

properties of the three phases of CO_2 for the range of temperatures of relevance to CO_2 dispersion from releases at sonic velocities, of interest to the CCS industry. This new equation of state has been developed in such a way that it is convenient for computational fluid dynamic (CFD) applications; the gas phase is computed from the Peng-Robinson equation of state (Peng and Robinson, 1976), and the liquid and condensed phases from tabulated data generated with the Span & Wagner equation of state (Span and Wagner, 1996) and the DIPPR® Project 801 database (http://www.aiche.org/dippr/), academic access to which can be gained through the Knovel library (http://why.knovel.com). Saturation pressure, gas and condensed phase densities, sound speed and internal energy have all been tabulated against temperature, providing the basis for a fully functional form for differentiation, interpolation and extrapolation in numerical simulations. No discontinuity or loss of accuracy at the critical point or anywhere along the saturation curve has been encountered by using this composite approach with different equations of state, as the authors have ensured that the Helmholtz free energy has continuous first derivatives.

2.3. Numerical Method

Following the same method as used previously (Wareing et al., 2012, 2013a, 2014; Woolley et al., 2013), the composite equation of state was implemented within a homogeneous equilibrium model into 'MG', an adaptive mesh refinement (AMR) RANS hydrodynamic method developed by Falle (1991). The method employs an upwind, conservative shock-capturing scheme and is able to employ multiple processors through parallelisation with the message passing interface (MPI) library. Integration proceeds according

to a second-order accurate Godunov method (Godunov, 1959). In this case, a Harten Lax van-Leer (van Leer, 1977; Harten et al., 1983) (HLL) Riemann solver was employed to aid the implementation of complex equations of state. The disadvantage of the HLL solver is that it is more diffusive for contact discontinuities; this is not important here since the contact discontinuities are in any case diffused by the artificial viscosity. The artificial viscosity is required to ensure shocks travel at the correct speed in all directions and is at a very low level, decreasing proportionally with increasing resolution.

2.4. Adaptive meshing strategy

The AMR method (Falle, 2005) employs an unstructured grid approach, requiring an order of magnitude less memory and giving an order of magnitude faster computation times than structured grid AMR. The two coarsest levels - 0 and 1 - cover the whole computational domain; finer grids need not do so. Refinement or derefinement depends on a given tolerance. Where there are steep gradients of variable magnitudes such as at flow boundaries or discontinuities such as at the Mach disc, this automated meshing strategy allows the mesh to be more refined than in areas of the free stream in the surrounding fluid. Each layer is generated from its predecessor by doubling the number of computational cells in each spatial direction. This technique enables the generation of fine grids in regions of high spatial and temporal variation, and conversely, relatively coarse grids where the flow field is numerically smooth. Defragmentation of the AMR grid in hardware memory was performed at every time-step, gaining further speed improvements for negligible cost through reallocation of cells into consecutive memory locations. The simulations presented below employed 5 levels of AMR and hence

a low level of artificial viscosity.

Steady state flows were achieved by running the simulations until the flow out of the top of the crater did not change and the integrated mass-flux out of the crater matched the integrated mass-flux into the crater from the point of release. The simulations presented hereafter are at this stage. The simulations are also convergent and show little variation with pressure, temperature and velocity at the puncture location.

3. Scenario 1: Side Puncture

3.1. Initial Conditions

In computationally modelling this puncture release, a three-dimensional Cartesian coordinate grid mesh was employed. Numerical simulations were performed employing the conditions listed in Table 1 as input conditions at the location of the puncture, modelled as a thin circular disk of diameter 25mm. These exit conditions were calculated by UCL as part of the COOLTRANS research programme. Other conditions were provided by DNV GL.

The initial state of the fluid in the rest of the domain consists entirely of stationary air at a pressure and temperature given in Table 1. Air is modelled via an ideal gas equation of state with $\gamma_a = 7/5$.

The crater was defined as a solid wall generated by a conical section above the mid-pipe level and cylindrical section below the mid-pipe level with the parameters given in Figure 1. The base of the cylindrical section sloped away from the pipe. The pipe was defined as a solid cylinder.

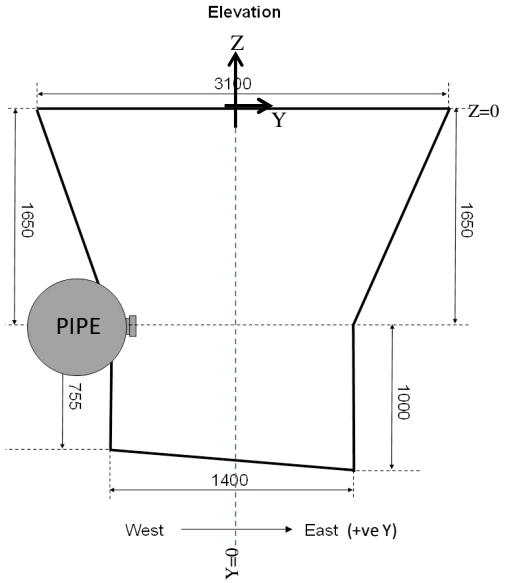

Figure 1: A cross-section of the pre-formed crater through the point of release constructed to surround the release location (Courtesy of DNV GL (Allason et al., 2012)).

A symmetry plane was imposed through the vertical axis of the puncture at $x = 0$ in order to reduce the computational effort required. This meant that only half the crater was modelled - when considering Figure 1 this symmetry plane is the plane of the page. This also meant that the effect of cross-wind was not modelled. We performed a number of test simulations with cross-winds, no cross-wind, a single symmetry axis and a double symmetry for those cases in which this was relevant and these showed that at the crater exit and just above it, the flow is moving fast enough that any cross-wind has a negligible effect, at least in this near-field region. All the other boundaries in the numerical domain were set to be free-flow, excepting that they only allow the in-flow of air with the initial atmospheric condition if any

in-flow occurs, for example as a result of a one-sided crater outflow dragging air into the crater from the other side. Hence the boundary conditions are adjusted to ensure that no CO_2 can flow into the domain. The conditions at the puncture location are enforced on every timestep.

3.2. Numerical Results

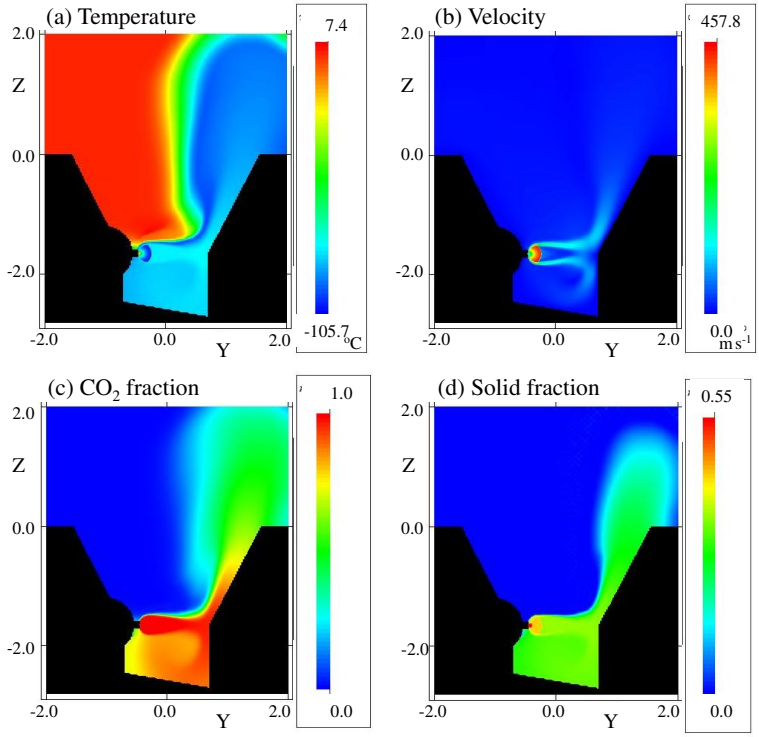

Figure 2: Predicted flow in a sideways puncture case on a slice at $x = 0$ through the middle of the crater. The colour scales are linear.

Figure 2 shows the predicted flow in the crater on a slice through the centre of the crater at the location of the puncture, parallel to the initial velocity vector at the puncture and on the same plane as Figure 1. The

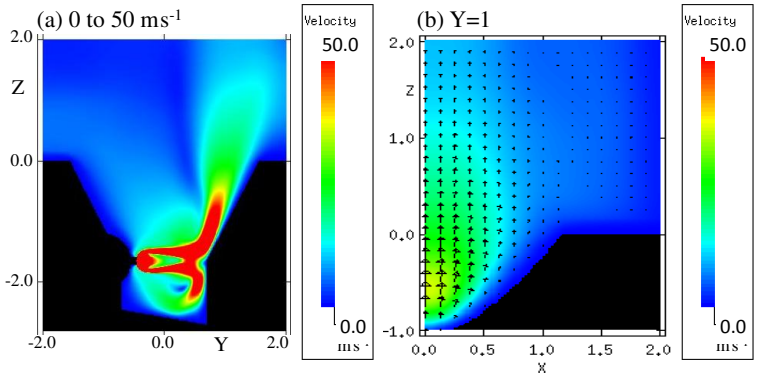

Figure 3: Velocities in the simulated flow on slices through the crater in a sideways puncture case; (a) on the slice at $x = 0$ and (b) on the slice $y = 1$ in the upper part of the crater. Length of vector arrow indicates relative magnitudes of velocity. The colour scales are linear.

expansion zone at the puncture caused by fluid exiting the high pressure reservoir is clearest in the plot of velocity, with high velocities just before the termination of the expansion zone by the Mach shock. The expansion zone also contains the coldest temperatures in the flow, around -105°C. Beyond the Mach shock, the temperatures are at the sublimation temperature as the homogeneous equilibrium model enforces the solid and gas phases to be in equilibrium and if the pressure is at atmospheric level, the temperature is the sublimation temperature of -78°C in pure CO_2 flow. The solid mass fraction just beyond the Mach shock is around 0.35. The core and sheath nature of the sonic jet is clear in the plot of velocity, where the slice through the jet shows the slow moving core post-Mach-shock surrounded by the fast moving sheath, before it impacts on the wall of the crater opposite the puncture. On impact, the flow is split up the wall and down into the bottom of the crater. The bottom of the crater (i.e. below the level of the puncture) contains a

cold cloud of CO_2 and air, although the mass fraction of air is relatively low at only 0.1 to 0.2. Approximately 35% of the CO_2 in the bottom of the crater is in the solid phase, implying a cloud temperature a few degrees below the sublimation temperature (as the cloud is not pure CO_2).

The flow going up the crater wall drags air in from the other side of the crater, mixing it into the flow, as can be seen more clearly in Figure 3, where panel (a) shows velocity on the same slice, but this time with a colour scale set on the interval from 0 to 50 $\mathrm{m\,s^{-1}}$ in order to elucidate the velocities at the top of the crater, which are around 25 $\mathrm{m\,s^{-1}}$ in the plume. Downwards flow of air into the crater is on the order of a few $\mathrm{m\,s^{-1}}$. It is also possible to identify recirculation in the bottom of the crater, as the CO_2 flows down the wall, back towards the puncture and is then both mixed back into the jet and moved upwards around the jet. In the righthand panel of Figure 3, a slice is shown at $y = 1$. This is a vertical slice at a right angle to the left panel, at a position $y = 1$ up the crater wall opposite to the puncture. The collimated jet nature of the flow going up the crater wall is clear and directed almost entirely vertically upwards in this plane.

Figure 4 shows the steady state flow at the crater edge ($z = 0$). The cold CO_2 flow is confined to the eastern half (upper half in the figure) of the top of the crater. The flow is up to 70% CO_2 with up to 28% of that in the solid phase in the centre of the release. The temperature is below the saturation temperature as 30% of the flow is mixed with air. The western half (lower half in the figure) consists of air being dragged into the crater at a velocity of a few metres per second. The flux integrations of this flow on this plane are reproduced in Table 2.

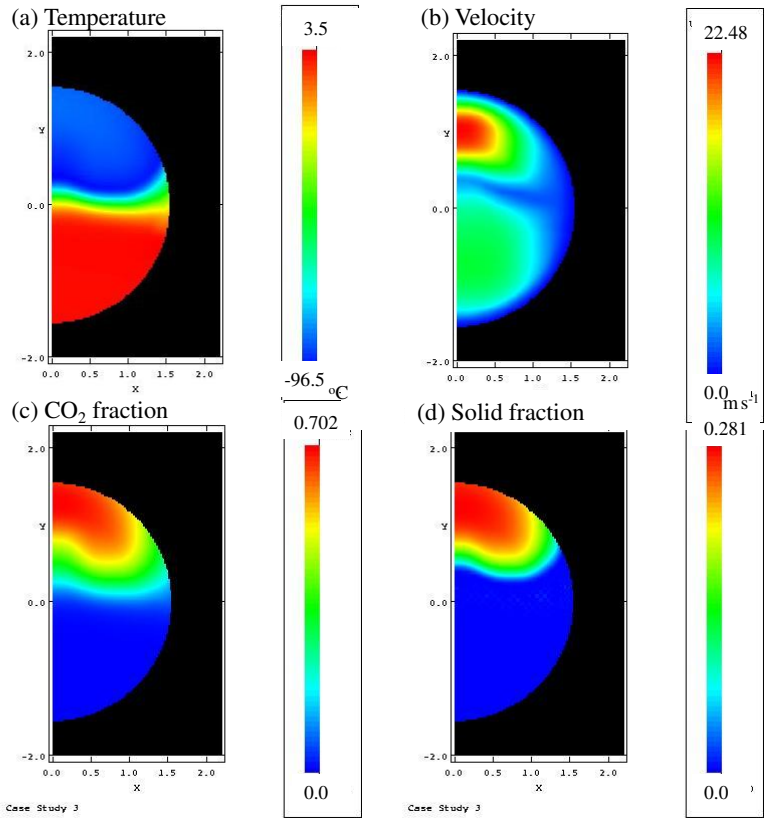

Figure 4: Plan view of simulated flow at the crater edge in sideways puncture case. The colour scales are linear.

In order to estimate particle deposition in the crater, we have taken these steady state flow conditions and then inserted particles and tracked their movement with a Lagrangian particle tracker. The particles are inserted in a hemisphere centred on the centre of the puncture and with a radius slightly larger than the distance from the Mach shock to the puncture along the jet axis. The particles are given velocities of 200 $\mathrm{m\,s^{-1}}$. These properties are set according to the particle properties at this location measured in recent laboratory scale experiments (Wareing et al., 2013b). These experiments

demonstrated that, in such releases, the particles are not in equilibrium and undergo an instantaneous pressure-driven (explosive) release in all directions. This particle insertion is set up to represent that situation. The movement of the particles is then computed, including the effect of drag, until the particles begin to leave the crater, and it is assumed that any particles that have hit the crater walls stick to them and are deposited in the crater. This is converted to a percentage of the original number of particles inserted into the flow and then scaled against the solid mass flux into the crater post Mach shock in order to obtain a rate of solid CO_2 mass deposition on the crater walls.

In the case of a sideways puncture, shown in Figure 5, the particles are dragged with the flow into the wall opposite the release point. Some particles hit the walls and stick whilst the majority are split up and down the wall opposite the puncture. Those moving up the wall head directly out of the crater. Those moving down the wall enter a recirculation back towards the release point and some are dragged back into the near-field of the jet, where once again a percentage hit the wall and stick. Experimentally, the walls of the crater have been observed to be frozen hard post release, which would fit with this description of particles hitting and sticking to the wall. Heat transfer is not considered in the current model. It would appear that the simple assumption used that particles stick and freeze the wall is suitable in this case, although heat transfer would be a next step for the model. The rate of particle deposition is presented in Table 3.

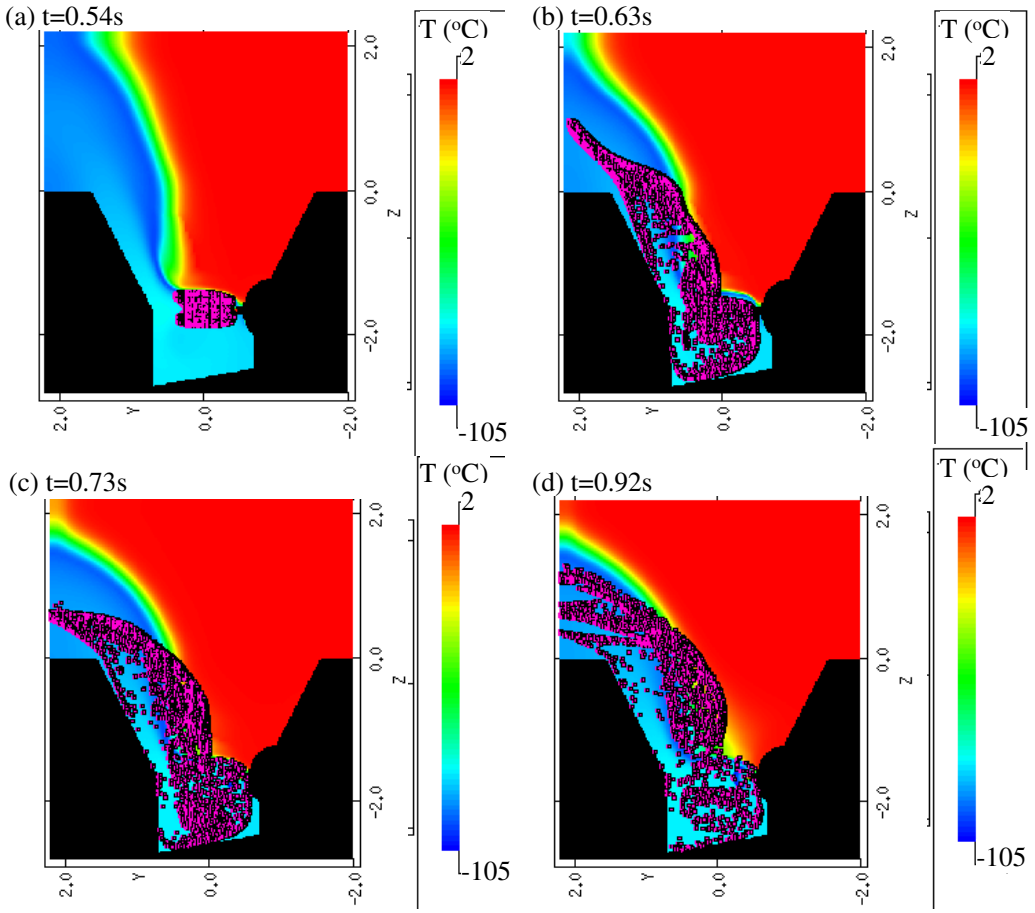

Figure 5: Snapshots of the flow on a vertical slice through the crater at the location of the puncture, parallel to the release direction, tracking the movement of particles in the flow. Particle locations are displayed as red squares. Particles stuck on the walls are inside the black regions. The colour scales are linear.

4. Comparison to Experimental Measurements

Experiments were carried out by DNV GL (Allason et al., 2012), under instruction from National Grid as part of the COOLTRANS programme of research (Cooper, 2012) in order to study how a puncture in a below ground

pipeline would behave. A length of pipeline used as a test section was kept pressurised during the experiment with dense phase CO_2 from a long length of approximately horizontal pipeline, forming a charge line. The test section had a bursting disk fitted to one side. In this particular experiment, the disk failed at a pressure of approximately 150 barg. When a valve was opened to the charge line, the driving pressure from a remote reservoir was used to pressurise the system and fail the bursting disk. The sideways release took place into a pre-formed crater (see Figure 1). The crater dimensions and shape were based on the crater formed in an earlier experiment in which the same release took place into a sandy soil backfill around the pipeline. There was no soil (backfill) in the crater in this particular experiment, so the release was initially taking place into air. The configuration resulted in a quasi-steady flow through the opening on the side of the pipe into the pre-formed crater. Measurements were made of the concentration and temperature within the CO_2 cloud that was produced, as it dispersed in the atmosphere.

A horizontal array of thermocouples was located on a supported frame at a height of 1m above the local ground level, directly above the crater. The arrangement of the temperature-measuring instruments in the horizontal frame suspended above the release location is shown in Figure 6. The centre of the array was aligned with the centre of the crater. In addition, measurements were made of the wind speed and direction at a number of locations. The ambient temperature and humidity were measured at a weather station within 500m of the release location.

The experiments were carried out in a similar manner to the venting tests that we have discussed previously Wareing et al. (2014). That is, the nitrogen

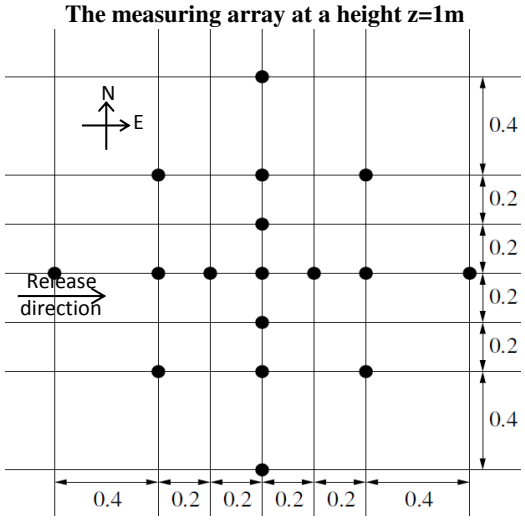

Figure 6: Locations of thermocouples on the measurement array located 1m above the pre-formed crater (Courtesy of DNV GL (Allason et al., 2012)).

reservoir was pressurised to a level above the guaranteed maximum failure pressure of the bursting disk (nominally 160 barg). The charge line and test section were filled with dense phase CO_2 to a pressure below the minimum guaranteed failure pressure of the bursting disk (nominally 135 barg). At a pre-set time, the valve separating the reservoir from the charge line was opened and the charge line and test section were gradually pressurised until the bursting disk failed. The pressure and temperature in the charge line were measured at the top of the line, within 2 or 3m of the check valve between the nitrogen and CO_2 systems. The time at which the nitrogen-CO_2 interface passed through the Coriolis meters employed could be detected from the instrument response and temperature in the line. The valves separating the charge line from the test section were then closed at this time, effectively terminating the useful dispersion measurements in the experiment.

Measurements of temperature were obtained on a plane 1m above the crater and it is against these data that the model performance will be compared. The experimental data have a variance on each measurement during the relevant time period of a degree or two. The temperature sensors are accurate over this range to within $\pm 5^{\circ}$C at worst, hence throughout experimental measurements are plotted with 5°C error bars, although this is considerably larger than the degree or two variance of the measurement of the relevant steady state time period of the jet (from 10 to 50 seconds into the release). The plotted temperature is the simple average for that particular sensor during the steady state period. The response time of the sensors is certainly less than the steady state period; from the sensor traces, it is possible to estimate that the response time to reach 80% of the temperature change is less than 5 seconds. Going from cold to hot following the release the response is considerably longer, due to possible ice formation around the connections, but this is beyond the steady-state period.

4.1. Comparisons

In Figure 7 the temperature predictions at 1m above the crater are compared to the experimental measurements on the same plane. The experimental data are presented time averaged from t=25 to t=50 seconds during the release. At later times, fall back of the plume appears to have a considerable effect on the experimental readings above the crater and this is not included in our model. In panel (a), the Northerly position of the sensors is ignored and the data collapsed onto the East-West centreline, where the numerical prediction is extracted from. Whilst the prediction does pass through the data, the data have a considerable spread which includes the prediction. A

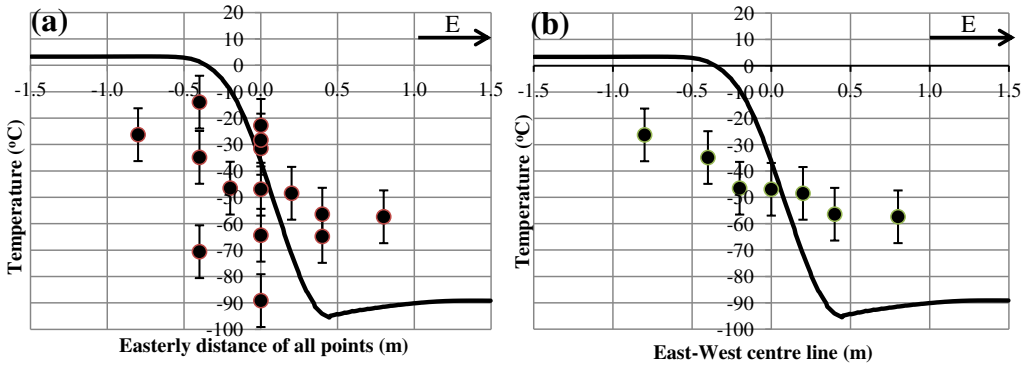

Figure 7: Comparison of predicted and experimentally measured (Allason et al., 2012) temperatures on the measuring array at 1m above ground for the puncture at the side of the pipeline scenario. (a) Centreline prediction compared to easterly position of all measuring array points. (b) A subset of these data showing only points on the East-West centreline.

subset of these datapoints are shown in panel (b), where only the datapoints on the true East-West centreline are shown. The experimentally observed datapoints don't show the same temperature range as the prediction, but do show the same trend, indicating broad agreement in the size of the cloud leaving the crater. Around 0m in Figure 7(b), it could be commented that the temperature is almost constant, but the trend across the entire data range is for higher temperatures in the West and lower temperatures in the East, which the prediction does show. The experimental data is very varied and turbulent and given that the RANS model does not capture this behaviour, the discrepancy between the data and prediction could be understood in this fashion. Further comparisons require higher quality data.

It is helpful to consider the measurements and data on a two-dimensional plane, rather than a one-dimensional slice. This is shown in Figure 8. As

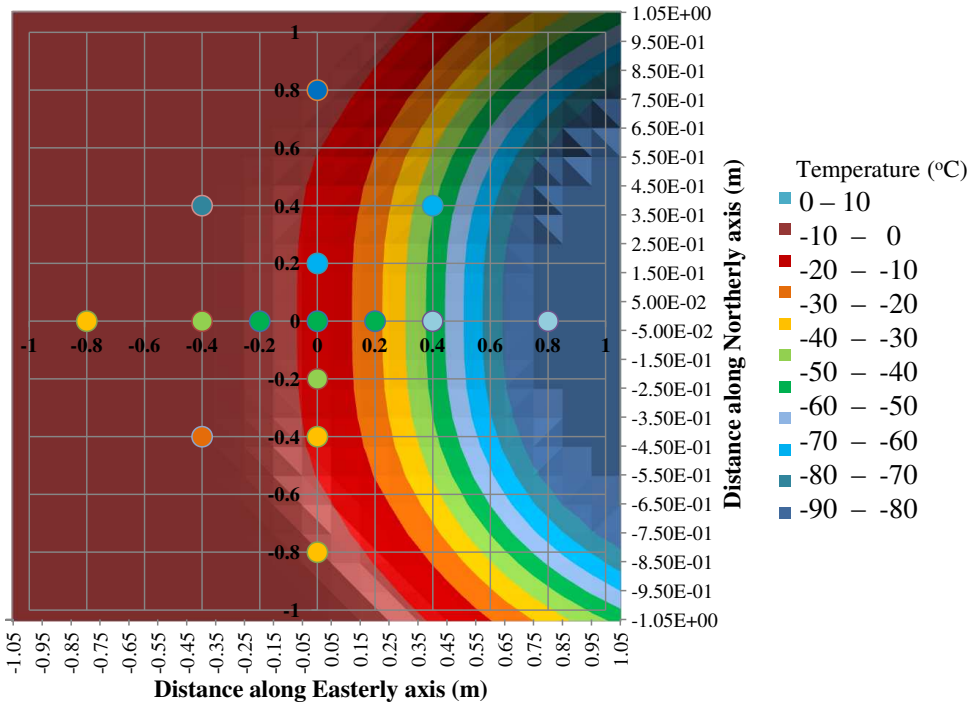

Figure 8: Comparison of predicted (contour colour plot) and experimentally measured (coloured data points (Allason et al., 2012)) temperatures on the measuring array at 1m above ground for the side puncture scenario.

can be seen from the figure, the coldest experimentally observed region is in the North-East quadrant and the warmest in the South-West. The coldest temperatures, range of temperatures and area of each region is in good agreement, even if the experimentally observed cloud coming out of the crater has been deflected away from the centreline of the crater.

The model is therefore able to predict the correct temperature range in the cloud coming out of the crater. The low temperatures in the cloud indicate that solid phase CO_2 is likely to be present. The model is also able to

predict the correct size of the release coming out of the crater, although the experimental measurements appear to be deflected away from the centreline of the crater through the release point. The atmospheric cross-wind on the day of the experiment was on average 0.7 $\mathrm{m\,s^{-1}}$ at 2m to 5m. As the cloud is moving upwards at approximately 20 $\mathrm{m\,s^{-1}}$, this cross-wind is unlikely to have a considerable effect only 1m above the crater. It is possible that deviations from the idealised conditions in the model, or large scale turbulence effects, could be responsible for this difference between prediction and experimental observation.

Photographic images of the experiment were also obtained (courtesy of DNV GL). Two stills from the video record are shown in Figure 9. In panel (a), at an early stage, the initial jet plume has reached a height of 15-20m (estimated by DNV GL). In panel (b), once the jet has reached a steady state, the height of the main plume is lower at approximately 10-15m, with a shallower cloud spreading around the release location. A two-dimensional test simulation using this model has predicted that a jet moving upwards with predicted conditions 1m below ground would reach an initial height around 18m and then, once a cold mixture of air and CO_2 is reentrained into the crater rather than ambient air, less energy is available to the jet and the plume height levels out post-reentrainment at approximately 12m. This simulation is in agreement with the observations and shown in Figure 10.

Figure 9: Photographs of the experimental release in the side puncture scenario at an early stage (a) and once steady state has been established (b) (Courtesy of DNV GL (Allason et al., 2012)).

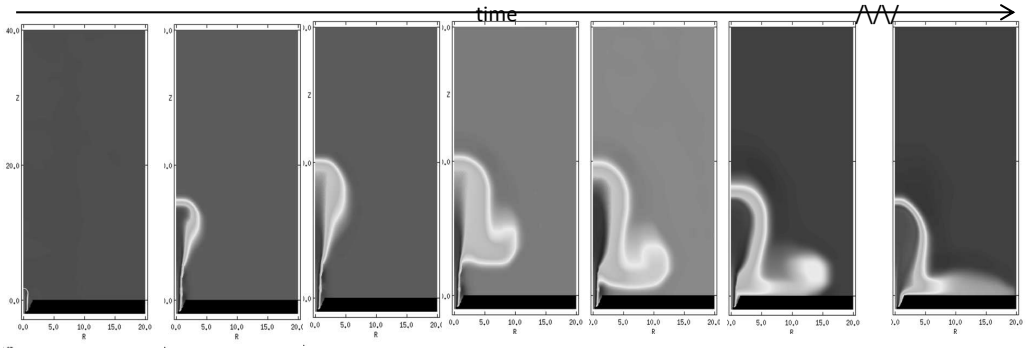

Figure 10: A two-dimensional simulation of a plume rising out of the crater following a puncture release. Time progresses from left to right showing the initial behaviour of the plume.

5. Scenario 2: Base Puncture

5.1. Initial Conditions

The puncture was idealised as a 25mm hole at the base of the pipeline, in the same manner as the previous scenario. This experiment took place with sandy soil backfill around the pipeline and was allowed to form its own

crater. The shape of the crater modelled in the numerical simulation was that measured after the experiment and the dimensions are shown in Figure 11. The crater was again defined as a solid wall in the numerical model and generated by a conical section above the level of the top of the pipe, this time with the cylindrical section below this level having the parameters as given in Figure 11. The base of the crater at the bottom of the cylindrical section was flat. The release conditions at the puncture were the same as in the previous scenario, shown in Table 1. The initial state of the fluid in the rest of the domain consists of stationary air at atmospheric pressure and a temperature of 10°C as recorded by atmospheric instrumentation at the time of the experimental test. There are no experimental measurements available for comparison in the near-field as the test was allowed to form its own crater. Air is modelled as previously.

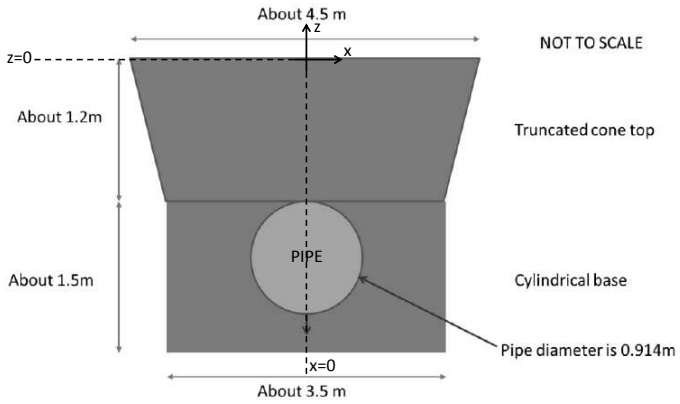

Figure 11: Details of the crater in the scenario with a puncture at the base of the pipeline (Courtesy of DNV GL (Allason et al., 2012)).

A symmetry plane was again imposed through the vertical axis of the puncture at $x = 0$ such that only half the crater was modelled - when consid-

ering Figure 11 this is at right angles to the plane of the page, through the vertical axis of the pipeline. All the other boundaries were set to free-flow, only allowing the in-flow of air with the initial atmospheric condition if any in-flow occurs as previously.

5.2. Numerical Results

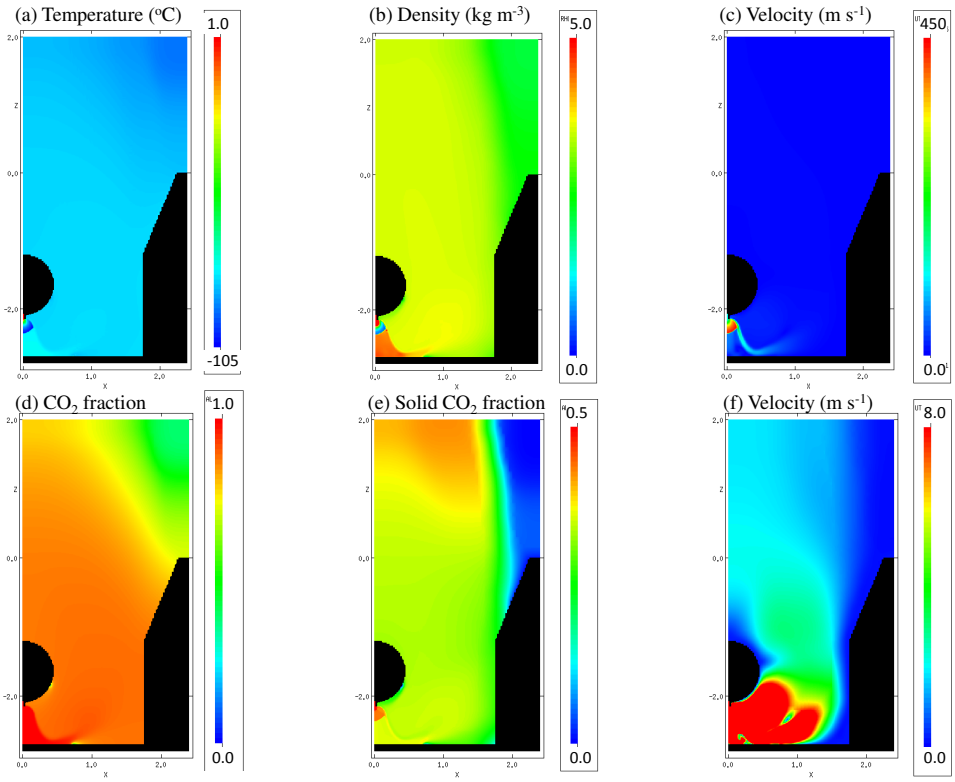

Figure 12: Vertical slices through the position of the puncture, perpendicular to the pipeline, showing the flow in the crater for the puncture at the base of the pipeline scenario. The colour scales are linear.

Figure 12 shows vertical slices through the simulated flow at the position of the puncture, perpendicular to the pipeline. The entire domain has been

filled by a cloud of cold CO_2. The downwards jet at the base of the pipeline is indicated by the position of the Mach shock, a short distance below the pipeline. The coldest temperatures and lowest densities are reached just before the Mach shock. The CO_2 fraction at this time is still 100%. As previously, post-Mach shock a jet forms pointing downwards, this time towards the base of the crater and consisting of a cold slow moving core surrounded by a fast moving sheath. This structure exists only for a very short distance as the jet impacts onto the base of the crater. It is deflected away from the middle of the base of the crater and towards the sides, where it then moves up the crater wall. Given that the entire momentum of the jet is downwards from the puncture and the base of the crater is flat and perpendicular to this, the high speed jet is transformed into a slow speed cloud filling up the crater and eventually spreading over the sides of the crater. There is no upwards plume in this prediction, just a cold cloud of CO_2 moving out of the crater at approximately 2 $\mathrm{m\,s^{-1}}$.

Figure 13 shows vertical slices through the simulated flow at the position of the puncture, but in this case parallel to the pipeline. The expansion zone of the release, terminated by the Mach shock, is clearly shown at the bottom of the middle of the pipeline. This vertical slice demonstrates the cylindrical symmetry of the Mach shock structure, as it appears very similar to Figure 12. It is possible to identify a region immediately above the pipeline in panel (f) where the velocity is zero. The implication of this is that the some of the soil immediately above the pipeline could remain there throughout the release, albeit frozen by the cold CO_2, as was observed in the experiment.

Figure 14 shows the flow coming out of the crater. This is on a horizontal

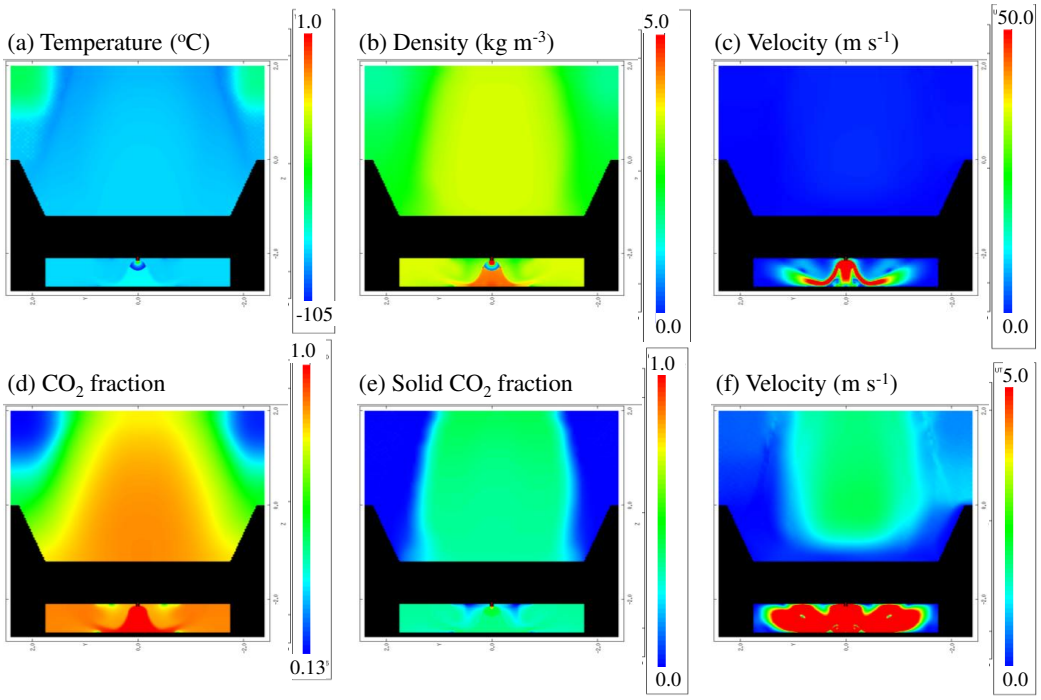

Figure 13: Further vertical slices through the position of the puncture, parallel to the pipeline, showing the flow in the crater for the puncture at the base of the pipeline scenario. The colour scales are linear.

plane at the crater edge ($z = 0$). The temperature of the flow is at or below the sublimation temperature, as the phases are in equilibrium and some air has been mixed in to the flow. The cloud is moving upwards at around 2 $\mathrm{m\,s^{-1}}$ in the centre of the crater dropping to zero at the rim. In the centre of the flow the cloud is over 85% CO_2, and 35% of that in the solid phase. The integrated fluxes for this flow on this plane are shown in Table 2.

Whilst there were no near-field measurements of this flow, video taken from a distance of a few hundred metres is available. Hence it is possible to compare this experiment with the video available from the side puncture

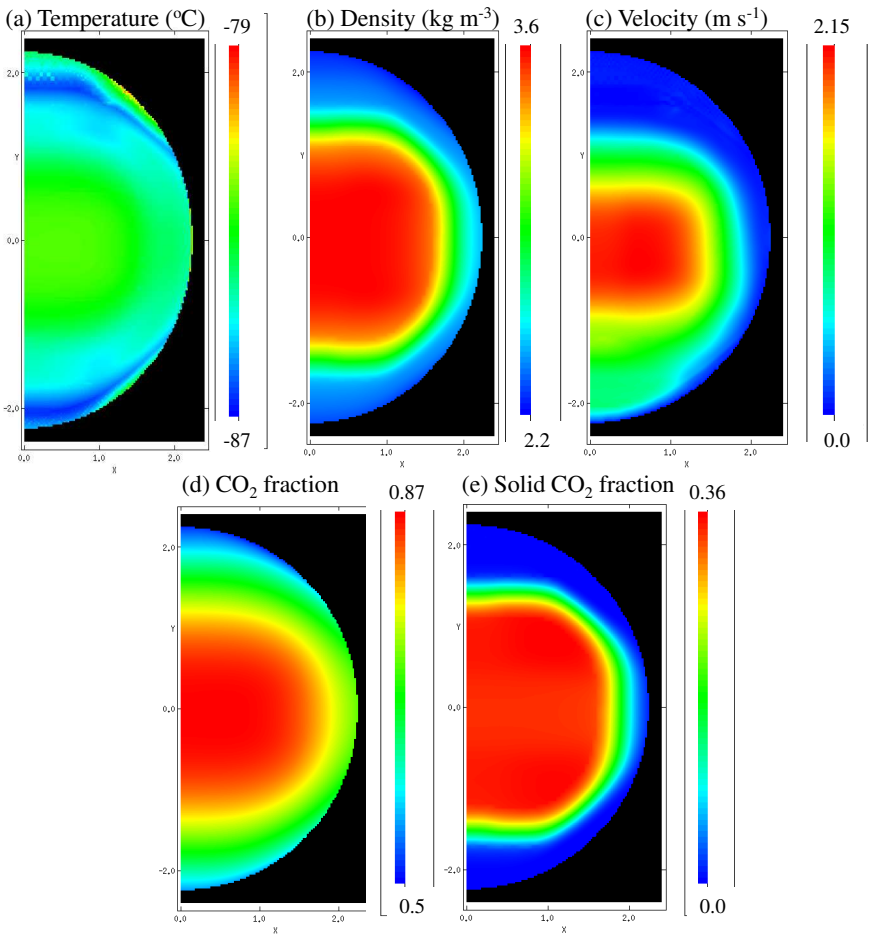

Figure 14: Horizontal planes at the crater edge, showing the flow at the crater rim for the puncture at the base of the pipeline scenario. The colour scales are linear.

case. The video reveals that a plume also forms in this scenario, although reaching a lower height than in the side puncture case. This plume reaches a variable height throughout the duration of the experiment, including periods where there is almost no plume above the surrounding cloud. No plume is predicted in this simulation - only a cold low-velocity cloud of CO_2.

Figure 15 shows the particle locations after the particles have been allowed

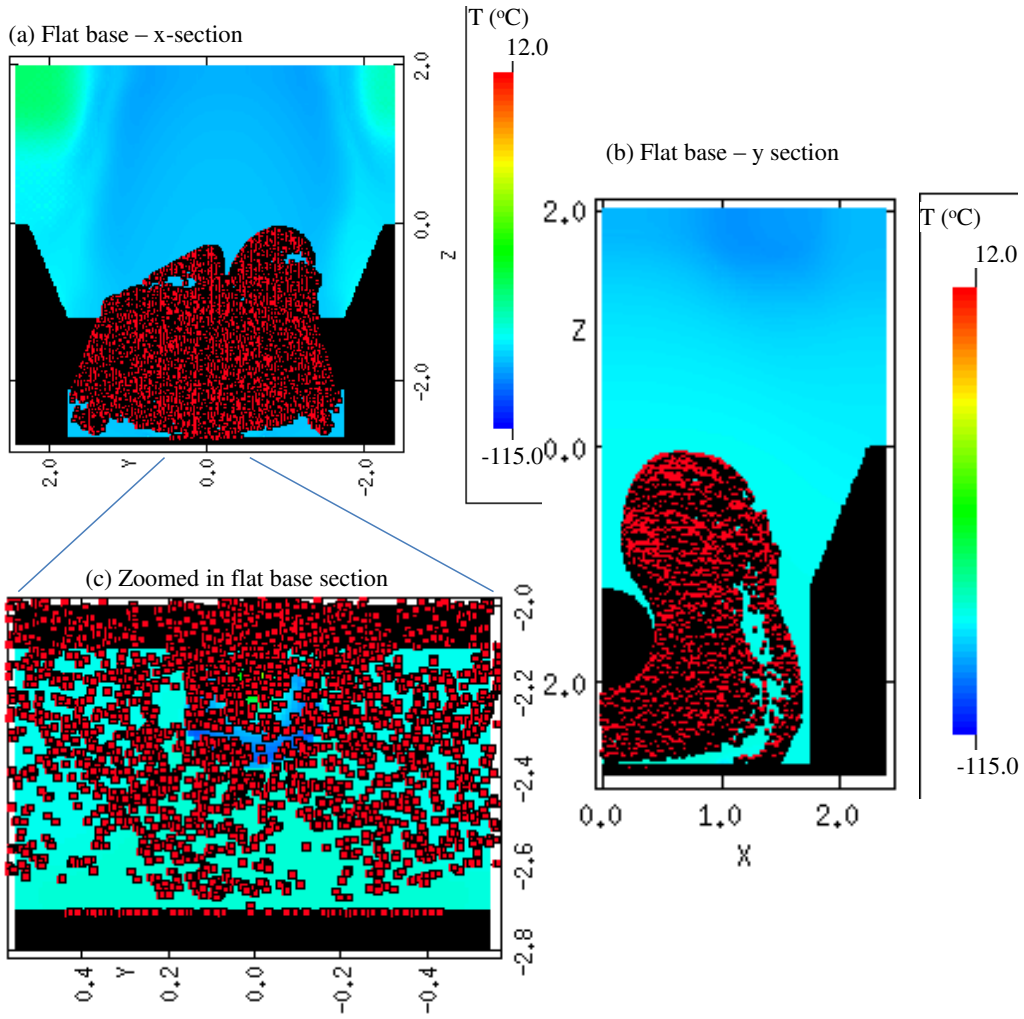

Figure 15: Base puncture scenario. A snapshot of the flow showing the particle deposition in the crater for the flat base crater. Particle locations are displayed as red squares. Particles stuck on the wall are inside the black regions. The colour scales are linear.

to move until they are approaching leaving the crater for this scenario. A large number of particles have been embedded into the flat base of the crater immediately below the puncture (see the zoomed in section shown in panel

(c)). This is where most, if not all, of the particles have been embedded onto the walls in this simulation.

Based on these particle tracking results, we implemented a revised model with a different shape to the base of the crater in order to investigate whether it is possible to obtain a faster plume flow of CO_2 from a puncture at the base of a pipeline. Specifically, a parabolic dish shape, raised in the centre to a point, achieved in the numerical model by the use of an inverted sine curve on the interval from 0 to $(\pi/2)$ scaled to the radius of the cylindrical section and rotated about the centre of the crater. The depth at the centre and sides differs from the depth mid-way between the two by 0.4m. This shape of crater base, whilst extreme, could be considered as one achieved when a frozen pile of solid CO_2 builds up below the puncture and in the stagnation points of the flow in the corners. The build-up of solid CO_2 in the form of a cone below an orthogonally impinging jet has been observed in previous experiments (Mazzoldi et al., 2008).

Figure 16 shows the results of this second simulation. Whilst the temperature in the resulting flow up the crater is similarly cold, the velocity of the flow up the crater is considerably larger - around five times more at 10 $\mathrm{m\,s^{-1}}$ at the crater edge. The faster flow also results in more air being mixed into the flow and less solid CO_2. The velocity is now on the order of that which will result in a plume going 10m or so above the crater, as observed in the experiment.

Figure 17 shows the predicted flow on a horizontal plane at the top of the crater. Again the CO_2 plume fills the crater, but this time moving upwards at a faster velocity - around 10 $\mathrm{m\,s^{-1}}$ in the core. The temperature is again

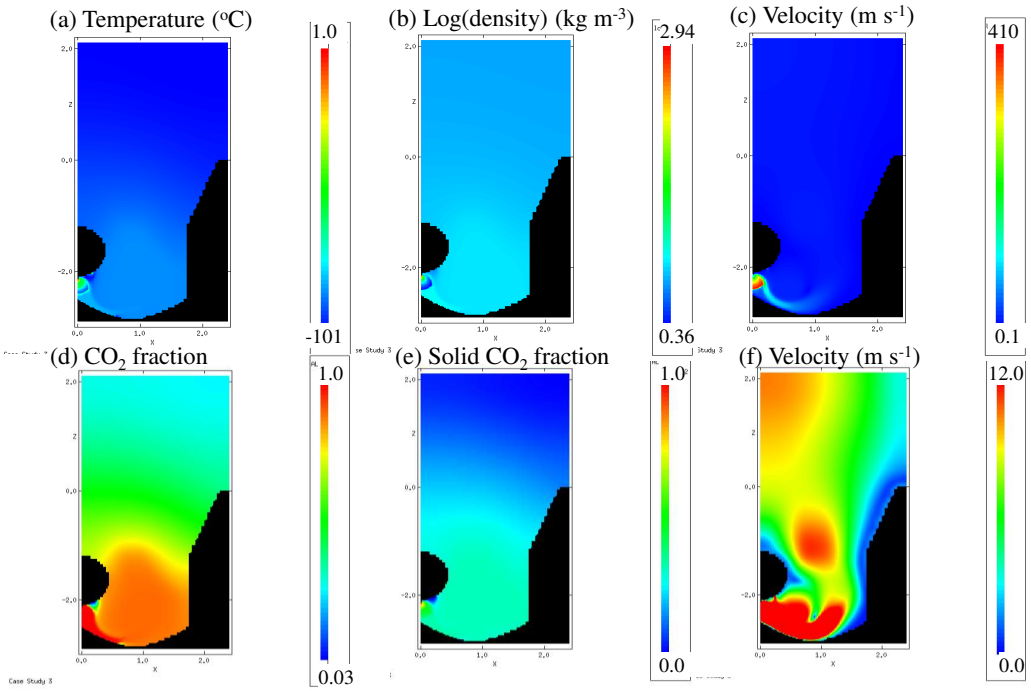

Figure 16: Vertical slices at the position of the puncture, perpendicular to the pipeline, showing the effect of a curved crater base in a modification to the crater shape in the base puncture scenario. The colour scales are linear.

below the sublimation temperature as air and CO_2 are present, but the CO_2 fraction is considerably less, peaking in the centre of the jet at only 50% compared to nearly 90% in the case of a crater with a flat base. The solid fraction is also half that in the flat-based crater case.

The simulated flow predicted from a curved crater base model better matches the observed experimental periods with a plume flow. It would be possible to further test the possibility of a curved crater base, as the CO_2 fractions at the crater rim are so different (by a factor of two) that far-field concentration measurements may be able to differentiate between the flat

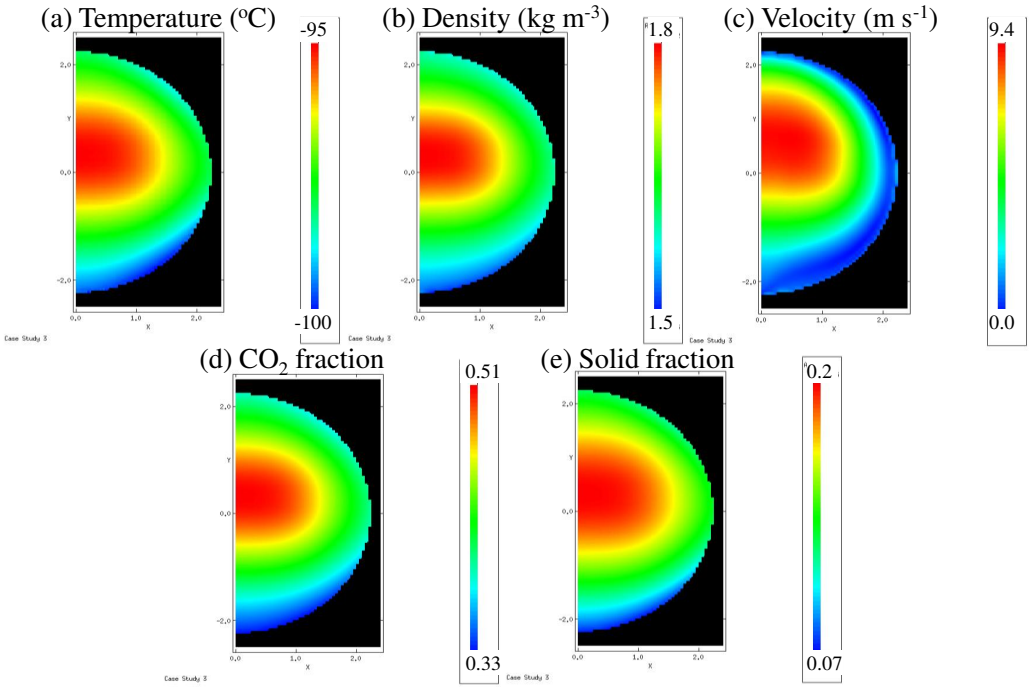

Figure 17: Horizontal planes at the crater edge, showing the flow out of a crater with a curved crater base in a modification to the crater shape in the base puncture scenario. The colour scales are linear.

and curved base models.

We also introduced particles to this second model, as shown in Figure 18. With a curved base, no particles were embedded below the nozzle and practically no particles embedded anywhere else in the crater. They were all transported out of the crater with the flow. This naively supports the argument for the curved base representing a pile of solid CO_2. A pile of solid CO_2 would not be observed experimentally unless direct observations of the crater were made very soon after the experiment. For safety reasons, this was not possible, but eyewitness accounts made shortly afterwards confirm

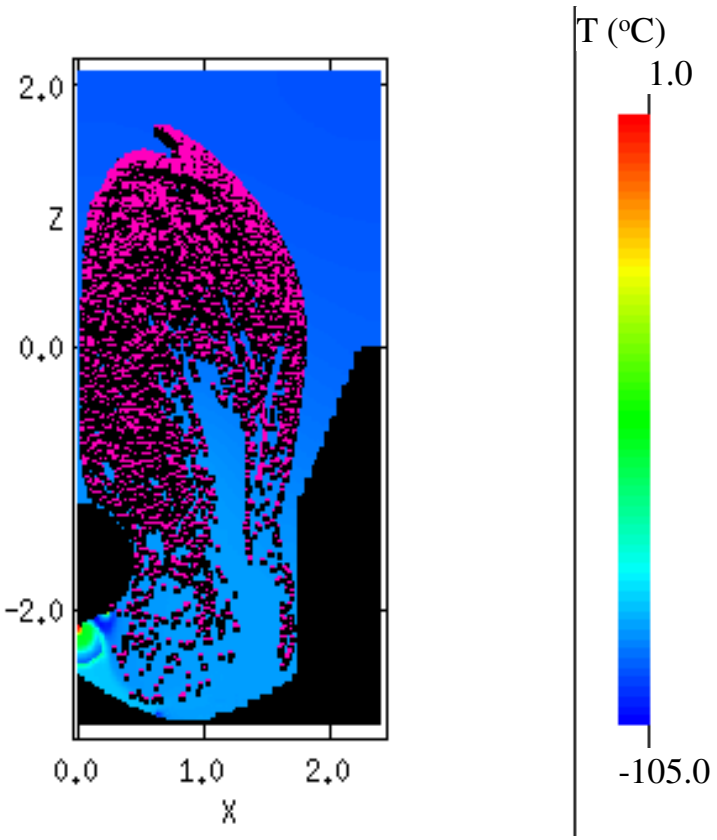

Figure 18: Base puncture scenario. A snapshot of the flow showing the particle deposition in the crater for the curved base crater. Particle locations are displayed as red squares. Particles stuck on the wall are inside the black regions. The colour scale is linear.

that there was more CO_2 deposited on the crater walls and the immediate vicinity of the crater than in the horizontal or vertically upward puncture experiments. Further, this pile of solid CO_2 which appears to deflect the flow out of the crater may have been destroyed or redistributed around the crater in the later stages of depressurisation.

As noted earlier, the experimentally observed height of the plume in this case is very variable. The cross-winds on the day of the experiment were

relatively high, so they may be responsible. This could also be an effect of reentrainment, but it could equally be an effect of build up of solid CO_2 directly below the puncture. Any height and volume variation in this pile of solid CO_2 would deviate the flow around it in different ways - the second model only considered a solid curved base which did not vary. It would be reasonable to expect variations in the shape of the base throughout a scenario with a puncture at the base of the pipeline, which would change the momentum in the flow (as shown by bracketing the two extremes with models presented here) and hence may change the mixing level and temperatures in the flow at the top of the crater.

6. Scenario 3: Top Puncture

6.1. Initial Conditions

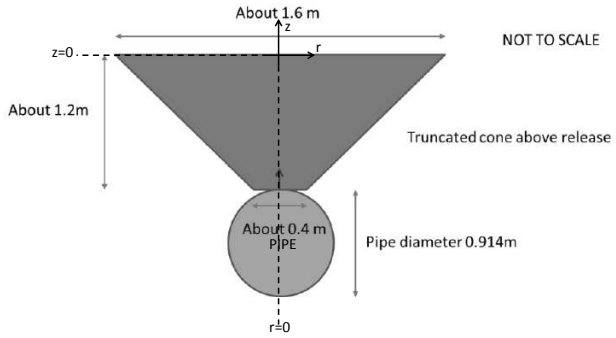

Figure 19: Details of the crater in the scenario with a puncture at the top of the pipeline (Courtesy of DNV GL (Allason et al., 2012)).

The puncture was idealised as a 25mm hole on the top of the pipeline, in the same manner as the previous scenarios. The idealised shape of the crater

used was based on a naturally-formed crater measured after an experiment and the dimensions are shown in Figure 19. The natural crater was unlike the earlier ones which had a rather regular shape. In this case, a rather rugged crater was formed, generally cone shaped but with a number of irregularities in the side walls immediately opposite and just above the release, with one prominent bulge where material had been eroded. The idealised crater was again defined as a solid wall in the numerical model generated by a conical section above the top-pipe level with the parameters given in Figure 19. Puncture release conditions were the same as the previous scenarios, as shown in Table 1. The initial state of the fluid in the rest of the domain consists of stationary air at atmospheric pressure and a temperature of 10°C as recorded by atmospheric instrumentation at the time of the experiment. Air is modelled as previously.

In this case, the model was implemented in two-dimensional axi-symmetry, with the vertical axis the cylindrical axis. The other boundaries were set to free-flow, only allowing the in-flow of air with the initial atmospheric condition if any in-flow was detected. The exit conditions in Table 1 are enforced on every step at the puncture.

6.2. Numerical Results

In Figure 20 we present the results of this simulation. The expansion zone terminated by the Mach shock is clear at the puncture. Beyond the Mach shock, the flow expands to fill the crater and is hence pure CO_2 until almost the crater rim. The temperature in the flow is at the sublimation temperature. The crater appears to act as a large expansion nozzle into which the flow expands and slows down to fill it post-Mach shock. Hence the

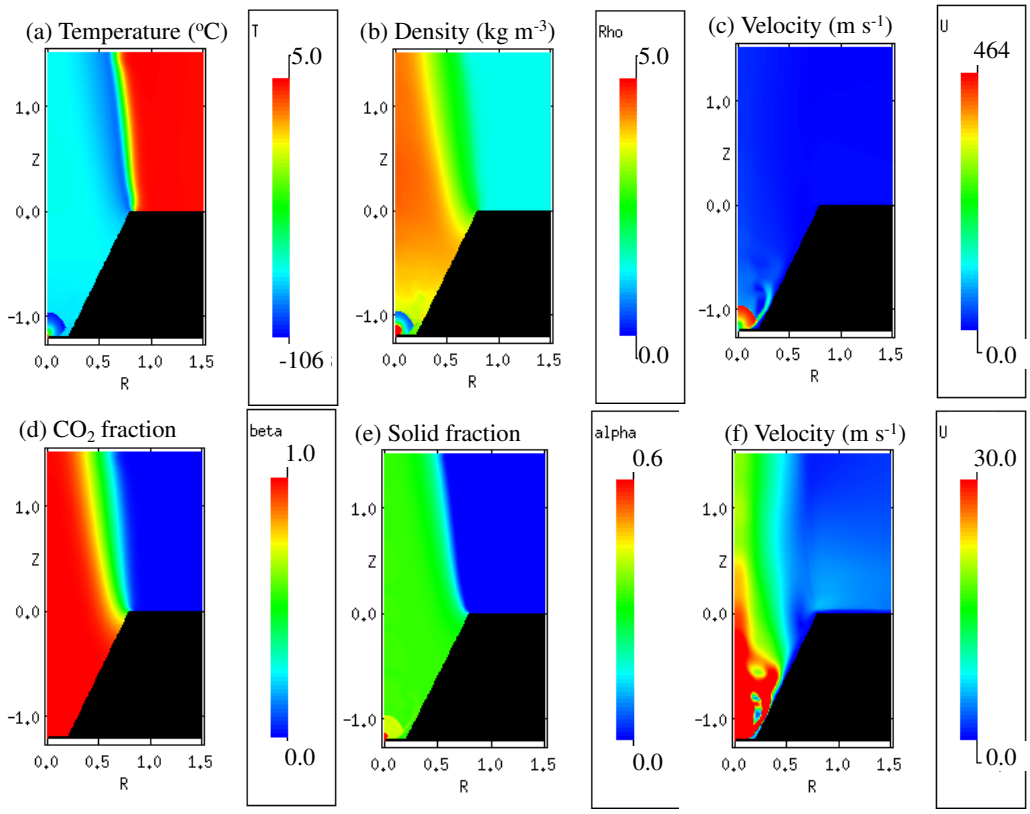

Figure 20: Vertical slices through the position of the puncture showing the flow in the crater for the puncture in the top of the pipeline scenario. The colour scales are linear.

flow contains 100% CO_2 just below the top of the crater, and approximately 35% solid fraction. The integrated fluxes for this flow on this plane are shown in Table 2. It is only at the rim of the crater where air is able to mix into the flow. The velocity of the flow at the crater edge is on the order of 28 $\mathrm{m\,s^{-1}}$ in the core, creating a large plume directly above the crater in agreement with photographic evidence from the experimental tests. This is of a magnitude not dissimilar to that numerically predicted for the sideways puncture. The experimental plume behaviour between the two tests is not

that different either, lending support to this prediction. Once the flow out of the crater begins to re-entrain cold air and CO_2 into the flow at the crater rim, rather than just ambient air as shown here, previous test simulations imply the height of the plume will fall by approximately 1/3. There is a slight pressure expansion at the crater rim, as the pressure is approximately 8% above atmospheric pressure, but this is not large and probably a consequence of the expansion nozzle nature of the crater.

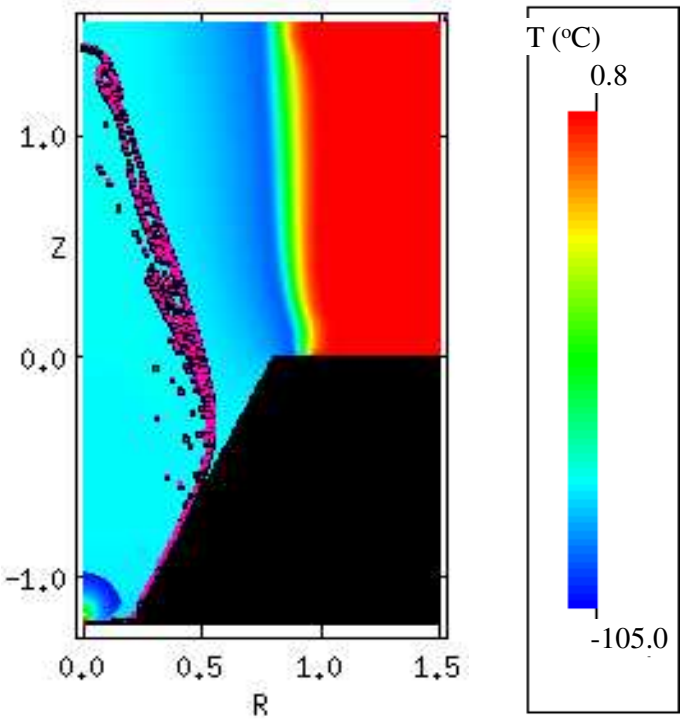

Figure 21: Top puncture case. A snapshot of the flow showing the particle deposition in the crater. Particle locations are displayed as red squares. Particles stuck in the wall are inside the black regions. The colour scale is linear.

Figure 21 shows the particle locations after the particles have been allowed to move with the flow until some are nearly leaving the computational

domain for the top puncture scenario. As before, the particles were inserted in a hemisphere around the Mach shock. In this case, a large number of particles have become embedded on the wall of the crater - almost 10% of the particles inserted into the simulation (see Table 3), which would seem a considerable proportion. Given the hemispherical introduction would have placed a number of particles close to the steep angled side wall at the base of the crater, this may be an effect of the particle introduction method, but it should be noted that particles are stuck on the wall all the way up the crater. As the crater is acting as a large expansion nozzle, it is not entirely surprising that particles have been driven by the expansion onto the walls. It is also interesting to note that in the experiment where the puncture was allowed to form its own crater, the walls of the crater were not an even conical section as idealised here. In fact (private communication with DNV GL), they were further dug outwards by the release, with more material removed from the crater and a shape in places more like a bulging conical section. The numerical predictions of particle behaviour would support the formation of such shapes through particle scouring of the side of the crater in the expansion up the crater.

7. Discussion

We have shown in the previous sections that the mathematical model described is capable of predicting flows out of craters as a result of a puncture of a buried high pressure pipeline of CO_2. Both qualitative data comparisons for all three scenarios - side puncture, base puncture and top puncture - are in agreement with available experimental data. Quantitative data comparisons

for the side puncture scenario have also shown good agreement, with justifications for the divergence between predicted and experimental rotations of the jet flow, even if the temperature ranges and size scales agree well.

In practice, depending on the capture technology, the transported CO_2 may contain different types of impurities. The major impact of this on dispersion modelling is in correctly calculating the thermodynamic decompression path and predicting accurate inlet conditions at the pipeline puncture, as initial conditions for the dispersion modelling. Our tests have shown that once correct inlet conditions are accounted for (typically considerably high pressures at the puncture), in a venting scenario this pure CO_2 dispersion model is able to reproduce measured temperatures reasonably well in the near-field dispersion of impure CO_2 (private COOLTRANS testing). The temperatures in the sonic flow are not considerably different to those observed in pure dispersion, whilst the impurities are at low levels (less than 5% in total). Of course high levels of impurity exist post-capture, but stringent pipeline inlet conditions may mean further purification at the point of capture before transport is required. Whichever is the case, improved equations of state are required for such modelling and these are in development for future modelling.

The introduction of atmospheric humidity will make a difference to these predictions. This will be limited to where air has been mixed into the flow, so not in the true near-field regions close to the sonic release and Mach shock. Once air and water vapour has been mixed into the flow, water ice will form in the low temperature environment and, since water has a latent heat of fusion greater than that of CO_2 (CO_2: 205 kJ/kg, water: 334 kJ/kg, values

obtained from the Knovel library physical property database), it will act as an energy sink causing the CO_2 jet to be less cold (in the order of a few degrees at most, depending on the level of humidity, COOLTRANS private communications). The jet formed will also be more buoyant.

Another source of uncertainty is in the thermophysical conditions imposed at the nozzle. Whilst these are reasonably well confined by experimental measurements in the pipework, there is some evidence that for certain conditions, phase stratification may occur vertically across the pipeline. This is unlikely to occur whilst there is still a driving pressure upstream, but downstream and once, in practical situations, any upstream emergency shutdown valves have been closed and the driving pressure ceases, this stratification may occur. At this time, since liquid will be at the bottom of the pipeline and gas at the top, release conditions at a base puncture may be very different - a different phase even - to those in a top puncture. Here we have modelled the worse case scenario, in line with the experiments performed, where the driving pressure continued throughout the puncture event. Further modelling accounting for such pipeline condition changes may shed further light on these different release types.

Models presented here have also indicated that solid deposition in the crater may change the shape of the crater base and influence the flow out of the crater, as inferred from observations during the experiments. Further work, in terms of numerical model development with solid deposition, two-way coupled to fluid flow, and experimental work, both full-scale and at laboratory scale with a crater where the flow can be better observed, is necessary to shed light on solid particle behaviour. Further models should

take this into account where flow prediction in and around the crater is a priority.

In the models presented here, particles hit crater walls and stick to the wall. There is no heat-transfer to the wall. In experiments, it would appear that the crater walls are frozen during these releases, so this is a suitable simple model that reproduces the observed freezing of the crater walls. A more refined model should include full particle-wall interaction, but would have to produce the same result.

The method used here employs a RANS numerical technique with a k-ϵ turbulence model. We have shown that this approach is suitable for free releases into air (Woolley et al., 2013; Wareing et al., 2014), however in this work we are considering flows that impact onto walls and undergo strong interactions with solid structures. A different turbulence model and/or numerical technique may give different results and it would be worthwhile exploring the use of other methods. Whilst k-ϵ was chosen to be used in the COOLTRANS research programme for smooth connection between partners in the flow and dispersion modelling, a Reynolds-stress based turbulence model would be more appropriate and that is undergoing development and validation for future application in this area.

8. Conclusions

This article has presented the application of a novel method for modelling sonic high pressure releases of dense phase CO_2 to the realistic scenario of punctures in a buried pipeline. Integrated fluxes have been produced for the flow out of the crater which can now be used for far-field dispersion

predictions and further quantified risk analysis.

Comparison made to limited available experimental data above the crater has shown that the model is capable of predicting temperatures in the flow in broad agreement with those data, obtained as part of the COOLTRANS programme of research (Cooper, 2012). Further qualitative comparisons for all three scenarios considered have indicated the predictions are showing similar plume behaviour to that experimentally observed. These near-field predictions have required a three-phase accurate equation of state, that also accounts for the latent heat of fusion.

Further experimental data at both laboratory-scale and larger scales is required to further validate the model and shed light on the behaviour of solid CO_2 in and around the crater, although we have used Lagrangian particle tracking methods and appropriate conditions derived from laboratory-scale experiments to estimate particle deposition in the crater in this work. Further work is also required to quantify the effect of impurities in the transported CO_2, the effect of the heat transfer to the crater walls and pipe and the effect of the more accurate turbulence modelling.

The escalation of a puncture event into a possible full-scale rupture of a buried pipeline will be considered in the next publication.

Acknowledgements

CJW was supported by the COOLTRANS Research Programme (Cooper, 2012) funded by National Grid, and CJW and MF would like to thank National Grid for their support of the work described herein. National Grid initiated the COOLTRANS research programme as part of the Don Valley

CCS Project in order to address knowledge gaps relating to the safe design and operation of onshore pipelines for transporting dense phase CO_2 from industrial emitters in the UK to storage sites offshore. The Don Valley CCS Project is co-financed by the European Union's European Energy Programme for Recovery (EEPR). The sole responsibility of this publication lies with the authors. The European Union is not responsible for any use that may be made of the information contained therein.

References

Allason, D., Armstrong, K., Cleaver, P., Halford, A., Barnett, J., 2012. Experimental studies of the behaviour of pressurised release of carbon dioxide. In: IChemE Symposium Series No. 158, IChemE. pp. 142–152.

Connolly, S., Cusco, L., 2007. Hazards from high pressure carbon dioxide releases during carbon dioxide sequestration processes. In: IChemE Symposium Series No. 153, IChemE. pp. 1–5.

Cooper, R., 2012. National Grid's COOLTRANS research programme. Journal of Pipeline Engineering 11, 155–172.

Cumber, P.S., Fairweather, M., Falle, S.A.E.G., Giddings, J.R., 1994. Predictions of the structure of turbulent, moderately underexpanded jets. Journal of Fluids Engineering 116, 707–713.

Cumber, P.S., Fairweather, M., Falle, S.A.E.G., Giddings, J.R., 1995. Predictions of the structure of turbulent, highly underexpanded jets. Journal of Fluids Engineering 117, 599–604.

Duncan, I.J., Wang, H., 1991. Estimating the likelihood of pipeline failure in CO_2 transmission pipelines: New insights on risks of carbon capture and storage. Int. J. Greenhouse Gas Control 21, 49–60.

Falle, S.A.E.G., 1991. Self-similar jets. Monthly Notices of the Royal Astronomical Society 250, 581–596.

Falle, S.A.E.G., 2005. AMR applied to non-linear elastodynamics, in: Plewa, T., Linde, T., Weirs, V.G. (Eds.), Proceedings of the Chicago Workshop on Adaptive Mesh Refinement Methods, Springer Lecture Notes in Computational Science and Engineering v.41, Springer, New York U.S.A.. pp. 235–253.

Godunov, S.K., 1959. A difference scheme for numerical computation of discontinuous solutions of equations of fluid dynamics. Matematicheskii Sbornik 47, 271–306.

Harten, A., Lax, P.D., van Leer, B., 1983. On upstream differencing and Godunov-type schemes for hyperbolic conservation laws. SIAM Review 25, 35–61.

Mazzoldi, A., Hill, T., Colls, J.J., 2008. CO_2 transportation for carbon capture and storage: Sublimation of carbon dioxide from a dry ice bank. Int. J. Greenhouse Gas Control 2, 210–218.

Peng, D.Y., Robinson, D.B., 1976. A new two-constant equation of state. Industrial and Engineering Chemistry: Fundamentals 15, 59–64.

Sarkar, S., Erlebacher, G., Hussaini, M.Y., Kreiss, H.O., 1991. The analysis

and modelling of dilatational terms in compressible turbulence. Journal of Fluid Mechanics 227, 473–493.

Span, R., Wagner, W., 1996. A new equation of state for carbon dioxide covering the fluid region from the triple-point temperature to 1100 K at pressures up to 800 MPa. Journal of Physical and Chemical Reference Data 25, 1509–1596.

van Leer, B., 1977. Towards the ultimate conservative difference scheme. IV. A new approach to numerical convection. Journal of Computational Physics 23, 276–299.

Wareing, C., Fairweather, M., Falle, S.A.E.G., Woolley, R.M., 2012. Reynolds-averaged Navier-Stokes modelling of sonic CO_2 jets, in: Hanjalic, K., Nagano, Y., Borello, D., Jakirlic, S. (Eds.), Proceedings of the 7th International Symposium on Turbulence, Heat and Mass Transfer, Begell House Inc., New York. pp. 349–512.

Wareing, C., Woolley, R.M., Fairweather, M., Falle, S.A.E.G., 2013a. A composite equation of state for the modelling of sonic carbon dixoide jets in carbon capture and storage scenarios. AIChE Journal 59, 3928–3942.

Wareing, C., Fairweather, M., Peakall, J., Keevil, G., Falle, S.A.E.G., Woolley, R.M., 2013b. Numerical modelling of particle-laden sonic CO_2 jets with experimental validation, in: Zeidan, D. (Ed.), AIP Conference Proceedings of the 11th International Conference of Numerical Analysis and Applied Mathematics, AIP Publishing. pp. 98–102.

Wareing, C., Fairweather, M., Falle, S.A.E.G., Woolley, R.M., 2014. Validation of a model of gas and dense phase CO_2 jet releases for carbon capture and storage application. Int. J. Greenhouse Gas Control 20, 254-271.

Wilday, A.J., McGillivray, A., Harper, P., Wardman, M., 2009. A comparison of hazard and risks for carbon dioxide and natural gas pipelines. In: IChemE Symposium Series No. 155, IChemE. pp. 392–398.

Woolley, R.M., Fairweather, M., Wareing, C.J., Falle, S.A.E.G., Proust, C., Hebrard, J., Jamois, D., 2013. Experimental measurement and Reynolds-averaged Navier-Stokes modelling of the near-field structure of multi-phase CO_2 jet releases. Int. J. Greenhouse Gas Control 18, 139–149.

Notation

Roman letters:

a	model parameter
b	model parameter
c	adiabatic sound speed
C	specific heat
d	non-dimensional nozzle diameter
e	total energy per unit volume
F	Helmholtz free energy
k	turbulence kinetic energy
m	mass
p	pressure
r	non-dimensional radial location
R	universal gas constant
t	time
S	entropy
T	temperature
u	magnitude of velocity
U	internal energy per unit mass
v	molar volume
w	molecular weight
z	non-dimensional axial location

Greek letters:

α	condensed phase fraction
β	total mass fraction of CO_2
δ	Peng-Robinson equation of state parameter
ϵ	dissipation rate of k
γ	ratio of specific heats
μ	molecular viscosity
ρ	density
τ	relaxation time
ω	acentric factor of the species

Subscripts:

0	reference state
a	air
c	condensed phase
crit	critical point
g	gas
i	initial
mix	mixture
s	saturation
trip	triple point
v	vapour

Table 1: Initial conditions for puncture simulations (Courtesy of UCL & DNV GL).

Section	Item	Value	Units
Release	Diameter of release	25	mm
	Outside diameter of test section	914	mm
	Wall thickness of test section	25.4	mm
	Depth of top of test section	1.2	m
	Composition	100%	CO_2
Atmospheric	Temperature	3.6	°C
	Relative humidity	81	%
	Average wind speed at 1m	0.61	$\mathrm{m\,s^{-1}}$
	Average wind speed at 4m	0.73	$\mathrm{m\,s^{-1}}$
	Average wind direction at 1m	260	degrees
	Average wind direction at 4m	255	degrees
Exit conditions	Pressure	3.564×10^6	Pa
	Temperature	274.0	K
	CO_2 fraction	100	%
	Liquid fraction	99.2	%
	Velocity	117.5	$\mathrm{m\,s^{-1}}$
	Mass-flow	51.9	$\mathrm{kg\,s^{-1}}$

Table 2: Integrated fluxes at ground level for all puncture scenarios. These are for a curved crater base in the case of a puncture at the pipeline base.

Type of puncture:	Side	Base	Top	[Units]
Total mass-flow up	67.2	109.0	51.4	$\mathrm{kg\,s^{-1}}$
Total mass-flow down	26.6	0.78	0.0	$\mathrm{kg\,s^{-1}}$
CO_2 mass-flow up	40.1	49.5	50.3	$\mathrm{kg\,s^{-1}}$
CO_2 mass-flow down	0.45	0.25	0.0	$\mathrm{kg\,s^{-1}}$
Solid mass-flow up	9.68	8.58	16.5	$\mathrm{kg\,s^{-1}}$
Solid mass-flow down	0.003	0.016	0.0	$\mathrm{kg\,s^{-1}}$
CO_2 fraction up	0.597	0.454	0.979	kg/kg
CO_2 fraction down	0.017	0.32	-	kg/kg
Solid fraction up	0.241	0.173	0.328	kg/kg
Solid fraction down	0.007	0.064	-	kg/kg
Total momentum up	912.0	629.5	757.4	$\mathrm{kg\,m\,s^{-2}}$
Total momentum down	136.8	0.23	0.0	$\mathrm{kg\,m\,s^{-2}}$
CO_2 momentum up	560.5	294.2	751.6	$\mathrm{kg\,m\,s^{-2}}$
CO_2 momentum down	1.62	0.074	0.0	$\mathrm{kg\,m\,s^{-2}}$
Solid momentum up	141.5	53.3	249.2	$\mathrm{kg\,m\,s^{-2}}$
Solid momentum down	0.001	0.005	0.0	$\mathrm{kg\,m\,s^{-2}}$
Inferred velocity up	13.57	5.77	14.74	$\mathrm{m\,s^{-1}}$
Inferred CO_2 velocity up	13.98	5.94	14.94	$\mathrm{m\,s^{-1}}$
Inferred solid velocity up	14.62	6.21	15.10	$\mathrm{m\,s^{-1}}$
Peak	22.48	9.4	27.8	$\mathrm{m\,s^{-1}}$
Flow-weighted temperature	179.73	176.5	195.2	K

Table 3: Particle deposition rates for the three puncture scenarios. Note that the particle deposition rate is calculated using the fact that post Mach shock, 35.5% of the CO_2 is in the solid phase and hence this is assumed to be the mass-flux of solid particles.

Scenario	Percentage of particles embedded in the walls %	Inflow rate $\mathrm{kg\,s^{-1}}$	Particle deposition rate $\mathrm{kg\,s^{-1}}$
Side puncture	1.0	50	0.1775
Base puncture, flat base	2.0	50	0.355
Base puncture, curved base	0.035	50	6.21×10^{-3}
Top puncture	9.5	50	1.68